VIRTUAL AND PHYSICAL PROTOTYPING
2026, VOL. 21, NO. 1, e2671497 (19 pages)
https://doi.org/10.1080/17452759.2026.2671497

Generative AI-guided in silico closed-loop optimisation of deposition morphology for 3D bioprinting applications

Colin Zhang, Kelum Chamara Manoj Lakmal Elvitigala and Shinji Sakai

Division of Chemical Engineering, Department of Materials Engineering Science, Graduate School of Engineering Science, The University of Osaka, Toyonaka, Japan

ABSTRACT

Recent advances in novel bioinks have dramatically increased the feasibility and applicability of 3D bioprinting for tissue engineering and regenerative medicine. However, developing new bioinks still requires extensive trial-and-error testing due to bioink rheology, crosslinking reactions, printing parameters, and limited resources. Previous classification- or regression-based AI models for bioink optimisation are typically black-box and cannot provide visual results. To address these challenges, a state-of-the-art disentangled and explainable generative AI framework was developed. The framework comprises a beta-conditional variational autoencoder (β-CVAE) for generating novel, variational images of printed constructs based on ink properties and printing parameters. Furthermore, an in silico closed-loop Bayesian optimisation (BO) system coupled with a convolutional neural network (CNN) was employed to quantitatively predict pre-printing performance and classify defects. The trained β-CVAE model can generate realistic and condition-dependent images of printed constructs. Visualisation of the latent space revealed an interpretable organisation of the learned features, supporting the model's explainability and controllability. Moreover, transfer learning was employed to rapidly adapt to new blueprint designs with limited data. Although this study focuses on acellular hydrogel printing, the bioink formulations and crosslinking conditions are cytocompatible and extensible to bioprinting applications. The proposed framework accelerates bioprinting optimisation through interpretable generative AI modelling.

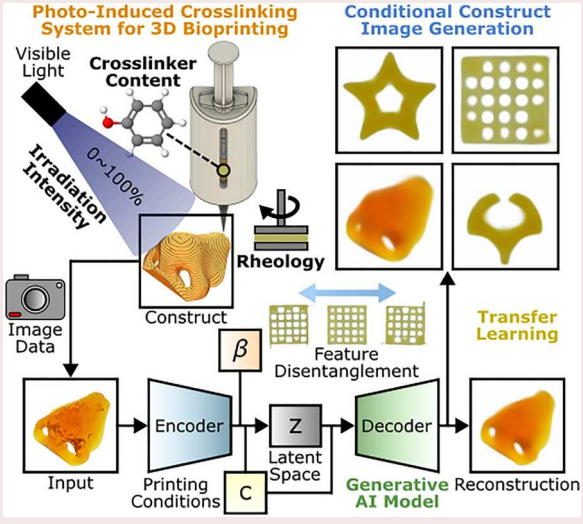

ARTICLE HISTORY
Received 14 March 2026
Accepted 5 May 2026

KEYWORDS
3D bioprinting; deposition morphology; machine learning; generative artificial intelligence; variational autoencoder

Highlights

- A generative AI model generates condition-dependent morphologies for 3D bioprinting applications.
- Latent visualisation suggests interpretable learned features, providing explainability and controllability.
- An in silico closed-loop Bayesian optimisation system evaluates and optimises printability.

CONTACT Shinji Sakai sakai@cheng.es.osaka-u.ac.jp Division of Chemical Engineering, Department of Materials Engineering Science, Graduate School of Engineering Science, The University of Osaka, 1-3 Machikaneyama-cho, Toyonaka, Osaka 560-8531, Japan

Supplemental data for this article can be accessed online at https://doi.org/10.1080/17452759.2026.2671497.

- Transfer learning adapted the generative model to new blueprints with limited data.

1. Introduction

Three-dimensional (3D) bioprinting is an evolving biofabrication platform that utilises advanced bioinks and bioprinting strategies to fabricate biomimetic tissues and organs for tissue engineering and regenerative medicine [1–3]. Extrusion-based 3D bioprinting is one of the most widely used methods due to its simplicity, affordability, and ability to process inks with a wide range of viscosities [4]. The method enables precise spatial placement of cell-laden bioinks to create complex and functional biostructures [5]. Recent advances in developing novel bioink formulations have significantly increased the feasibility of applying 3D bioprinting technologies for the fabrication of functional living tissues and personalised medicine [6,7]. However, developing novel bioinks often involves conducting repetitive, tedious experiments to ensure the ink formulations achieve optimal printing performance [8,9]. This leads to one of the main challenges in quality control for 3D bioprinting: optimising printability, or shape fidelity, such that printed structures accurately match the computer-aided design (CAD) model [10]. Printability is influenced by numerous factors, including the rheological properties of bioinks, the chemistry of crosslinking systems, and operational parameters of the printer [11,12]. As a result, predictive methods are essential for reducing trial-and-error iterations and effectively identifying the relevant printing window.

Recent studies have introduced methods that employ numerical simulations and machine learning (ML) to predict and assess printability [13–15]. For example, computational fluid dynamics (CFD) simulations have been used to examine the effects of printing speed, nozzle height, flow rate, and rheology on filament and deposition morphology in extrusion-based 3D bioprinting [16,17]. While CFD simulations provide a mechanistic understanding, they can be computationally demanding and sensitive to complex model assumptions [18]. In parallel, ML, particularly deep learning (DL), has been applied to classify printing defects and predict quantitative printability scores [19]. A previous study employed in situ vision systems powered by convolutional neural networks (CNNs) to detect layer-wise anomalies and geometric defects in extrusion-based 3D bioprinting [20]. A subsequent study reported a CNN-based closed-loop extrusion bioprinting framework that automatically classifies and corrects over- and under-extrusion errors in real time [21]. Another study employed a regression-based CNN coupled with a novel Hausdorff distance (HD) metric to predict the printability of printed constructs against the ideal CAD model [22]. Beyond vision-based defect detection, a temporal convolutional network-long short-term memory (TCN-LSTM) model trained on time-series sensor data achieved ink-insensitive prediction of deposition linewidth across various biomaterial inks [23]. Another study implemented a hybrid artificial neural network-finite element analysis (ANN-FEA) framework to predict the Young's modulus of 3D-printed bone scaffolds [24]. Although classification and regression predictions improve the bioink screening process, they are typically black-box models and do not directly provide visual printing results, and the scarcity of datasets often limits their performance and effectiveness. In contrast, disentangled generative models serve as a complementary approach to predictive models. They enhance explainability by visualising latent variables and help fill data gaps by generating realistic images and enlarging the dataset.

Generative artificial intelligence (AI) has received widespread attention for its ability to learn from representative datasets and generate complex outputs, including text, images, videos, 3D structures, and molecular graphs [25–27]. For example, conditional generative adversarial networks (GANs) have enabled inverse design of 3D mechanical metamaterials with targeted static and dynamic properties through generating novel samples [28]. Although GANs can produce sharp samples, they are increasingly criticised for their susceptibility to training instabilities and mode collapse, which lead to less diverse outputs [29]. On the other hand, variational autoencoders (VAEs) are a class of generative AI models that learn a probabilistic mapping from high-dimensional data, such as images, to a compact, low-dimensional latent representation; VAEs are typically more stable to train and support physically meaningful interpolation [30,31]. VAE-based models have been applied to de novo molecular design for generating molecules that satisfy multiple target properties beyond the training range [32,33]. Despite the rapid progress and deployment of generative AI, its potential in 3D bioprinting remains largely unexamined.

The present study focuses on acellular hydrogel printing as a foundational step for generative AI-guided cell-laden 3D bioprinting. A state-of-the-art beta-conditional variational autoencoder (β-CVAE) was implemented to generate deposition morphology for extrusion-based 3D bioprinting under conditional constraints. This generative model was trained on images of printed grid structures produced using a visible-light-crosslinking system comprising alginate-phenol (ALG-Ph) and hyaluronic acid-phenol (HA-Ph) conjugated inks with Tris(bipyridine)ruthenium(II) chloride ($[Ru(bpy)_3]^{2+}$) and

sodium persulfate ($Na_2S_2O_8$; SPS). Crosslinking is achieved via the Ru/SPS-mediated photoredox process, in which visible light excites $[Ru(bpy)_3]^{2+}$, triggering persulfate activation and subsequent phenol-phenol coupling [34]. The model was conditioned on key parameters that influence printing quality: rheological properties, irradiation intensity, and phenolic content. Additionally, support vector regression (SVR) was used as a surrogate model to predict rheological parameters of ALG-Ph and HA-Ph inks from ink compositions. Furthermore, an in silico closed-loop Bayesian optimisation (BO) system, integrated with a multi-task CNN, was developed to classify, evaluate, and optimise the printability of the generated deposition morphology across varying irradiation intensities.

The proposed generative AI framework can generate novel, variational images of deposition morphologies consistent with experimental observations, thereby helping optimise ink formulations and operating conditions with fewer experimental iterations. The latent space of the trained β-CVAE model showed high disentanglement in learned features, highlighting the model's robustness, explainability, and controllability. Moreover, transfer learning was leveraged to generate images of new blueprint designs by fine-tuning the pretrained β-CVAE on small, domain-specific datasets. Concurrently, these capabilities establish a first step toward utilising generative AI as a design and screening tool in 3D bioprinting, facilitating data-efficient exploration of bioink development and optimisation.

2. Results

2.1. Overview of 3D bioprinting system and generative AI model

This study aims to conditionally generate images of printed constructs based on rheological and chemical properties of inks used in a visible-light-induced 3D bioprinting system (Figure 1a). The dimensions and printing time of the blueprints utilised in this study are presented in Figure S1. Constructs were fabricated via layer-by-layer extrusion and crosslinked under 450 nm irradiation at varying intensities. Images of the constructs were acquired, and image segmentation was used to remove background noise. Influential factors that can affect the deposition morphology in such a system include rheological properties, crosslinker (phenolic group) content, and irradiation intensity (Figure 1b). The generative AI framework employs a β-CVAE, which is a novel disentangled and conditional generative model that balances reconstruction accuracy and latent space regularisation through the hyperparameter β [35].

The β-CVAE architecture comprises an encoder and a decoder, which are CNNs with learnable parameters ϕ and θ, respectively (Figure 1c). The input image $\boldsymbol{x}$ is processed by the encoder's convolutional layers, outputting mean $\boldsymbol{\mu}$ and standard deviation $\boldsymbol{\sigma}$ vectors. The condition vector c is concatenated with the encoder output. These define the approximate posterior (encoder) distribution $q_\phi(\boldsymbol{z}|\boldsymbol{x}, \boldsymbol{c})$ as a Gaussian distribution $\mathcal{N}(\boldsymbol{\mu}, \boldsymbol{\Sigma})$ with mean $\boldsymbol{\mu}$ and a diagonal covariance matrix $\boldsymbol{\Sigma}$ whose diagonal entries are the variances $\boldsymbol{\sigma}^2$. The latent variable z is sampled from $\mathcal{N}(\boldsymbol{\mu}, \boldsymbol{\Sigma})$ using the reparameterization trick:

$$\boldsymbol{z} = \boldsymbol{\mu} + \boldsymbol{\sigma} \odot \epsilon \tag{1}$$

where $\epsilon \sim \mathcal{N}(\boldsymbol{0}, \boldsymbol{I})$ is a random noise vector, and $\odot$ represents element-wise multiplication. This trick enables model learning by allowing gradient flow through sampling, as z is treated as a deterministic function of $\boldsymbol{\mu}$, $\boldsymbol{\sigma}$, and ϵ.

The image $\boldsymbol{x}'$ is reconstructed from $\boldsymbol{z}$ and $\boldsymbol{c}$ by the decoder network using bilinear upsampling layers. The model is trained by minimising the negative evidence lower bound (ELBO), referred to here as the β-CVAE loss function:

$$\begin{aligned}\mathcal{L}_{\beta\text{-CVAE}} = &-\mathbb{E}_{q_\phi(\boldsymbol{z}|\boldsymbol{x},\boldsymbol{c})}[\log p_\theta(\boldsymbol{x}|\boldsymbol{z}, \boldsymbol{c})] \\ &+ \beta D_{\mathrm{KL}}(q_\phi(\boldsymbol{z}|\boldsymbol{x}, \boldsymbol{c}) \,||\, p(\boldsymbol{z}))\end{aligned} \tag{2}$$

The first term on the right-hand side (reconstruction loss) in Eq. (2) is the negative average log-likelihood of the input x under the decoder distribution $p_\theta(\boldsymbol{x}|\boldsymbol{z}, \boldsymbol{c})$, conditioned on $\boldsymbol{z}$ and $\boldsymbol{c}$. The expectation $\mathbb{E}_{q_\phi(\boldsymbol{z}|\boldsymbol{x},\boldsymbol{c})}$ denotes an average over $\boldsymbol{z}$ sampled from $q_\phi(\boldsymbol{z}|\boldsymbol{x}, \boldsymbol{c})$. As $p_\theta(\boldsymbol{x}|\boldsymbol{z}, \boldsymbol{c})$ is assumed to be an isotropic Gaussian with mean x' and identity covariance $\boldsymbol{I}$, the reconstruction loss can be approximated as:

$$-\mathbb{E}_{q_\phi(\boldsymbol{z}|\boldsymbol{x},\boldsymbol{c})}[\log p_\theta(\boldsymbol{x}|\boldsymbol{z}, \boldsymbol{c})] \approx \mathbb{E}_{q_\phi(\boldsymbol{z}\,|\boldsymbol{x},\boldsymbol{c})}[||\boldsymbol{x} - \boldsymbol{x}'||^2] \tag{3}$$

which represents the mean squared error (MSE) between the input $\boldsymbol{x}$ and reconstruction $\boldsymbol{x}'$.

The second term on the right-hand side (Kullback-Leibler (KL) divergence) in Eq. (2) measures the difference between $q_\phi(\boldsymbol{z}|\boldsymbol{x}, \boldsymbol{c})$ and a prior $p(\boldsymbol{z})$ that is treated as a standard normal distribution $\mathcal{N}(\boldsymbol{0}, \boldsymbol{I})$. The hyperparameter β controls the balance between reconstruction accuracy and the proximity of $q_\phi(\boldsymbol{z}|\boldsymbol{x}, \boldsymbol{c})$ to $p(\boldsymbol{z})$. The KL divergence is computed analytically as:

$$D_{\mathrm{KL}}(q_\phi(\boldsymbol{z}|\boldsymbol{x}, \boldsymbol{c}) \,||\, p(\boldsymbol{z})) = \frac{1}{2}\sum_{j=1}^{d}(\mu_j^2 + \sigma_j^2 - 1 - \log \sigma_j^2) \tag{4}$$

where d is the latent space dimensionality, μ_j is the j-th component of $\boldsymbol{\mu}$, and σ_j^2 is the j-th component of the variance vector $\boldsymbol{\sigma}^2$. By encouraging $q_\phi(\boldsymbol{z}, \boldsymbol{x}, \boldsymbol{c})$ to match $p(\boldsymbol{z})$, the KL divergence ensures that z sampled from $p(\boldsymbol{z})$ during generation lie within regions the decoder has learned to reconstruct, enabling coherent image generation.

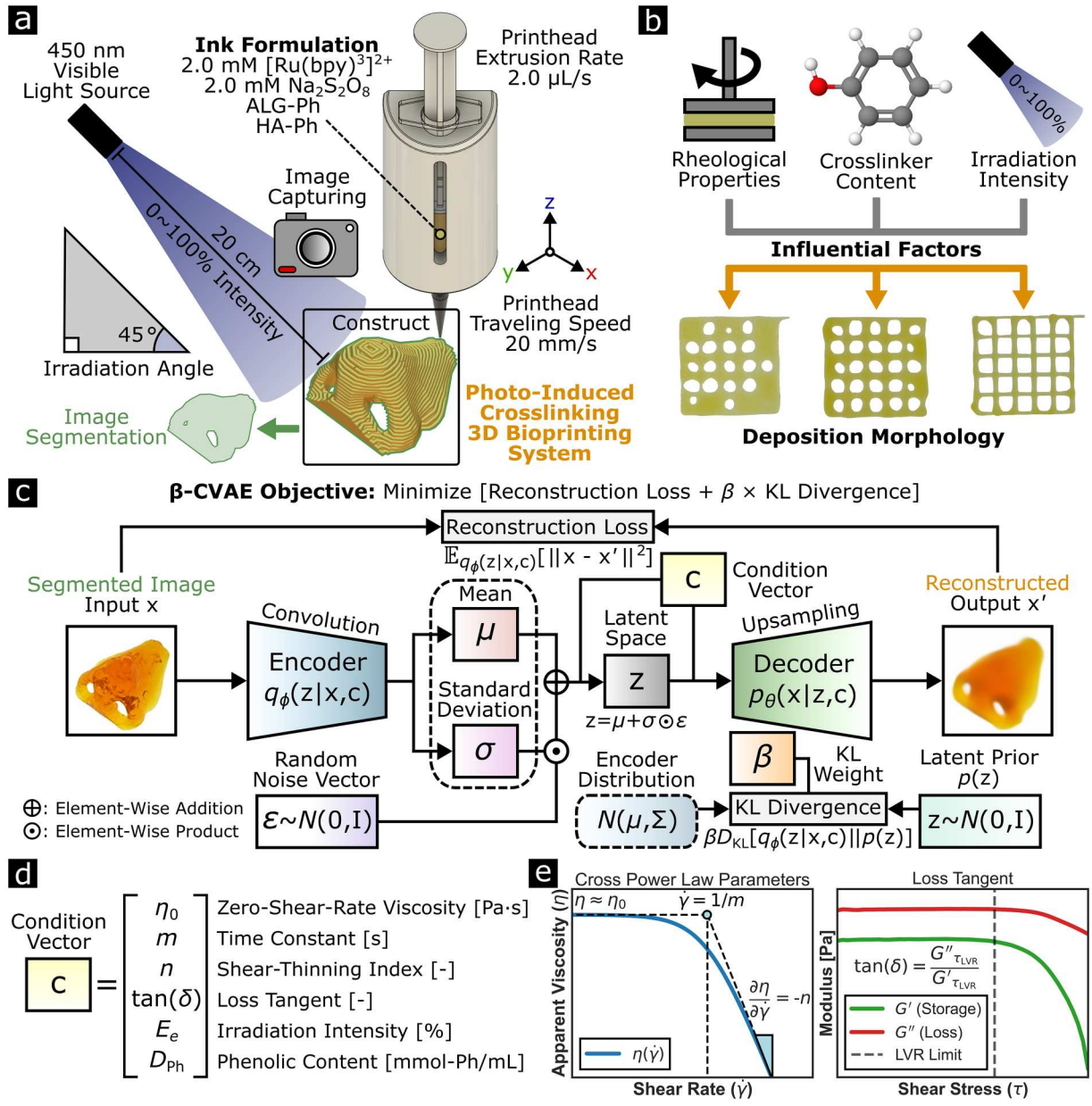

Figure 1. Disentangled generative AI framework for 3D bioprinting. (a) The visible-light-induced bioprinting system consists of alginate-phenol (ALG-Ph) and hyaluronic acid-phenol (HA-Ph) composite inks containing Tris(bipyridine)ruthenium(II) chloride ($[Ru(bpy)_3]^{2+}$) and sodium persulfate ($Na_2S_2O_8$). (b) Influential factors that govern deposition morphology for the visible-light-induced bioprinting system. (c) The beta-conditional variational autoencoder (β-CVAE) encodes the condition vector ***c*** and images of printed constructs into latent distributions and reconstructs the images by sampling from them while minimising the sum of reconstruction loss and Kullback-Leibler (KL) divergence. (d) The condition vector ***c*** contains six rheological and processing descriptors. (e) The Cross Power Law for modelling a shear-rate-dependent viscosity curve, and the definition of tan (δ) based on storage modulus (G') and loss modulus (G'') within the linear viscoelastic region (LVR).

The condition vector consists of six descriptors: zero-shear-rate viscosity (η_0), time constant (m), shear-thinning index (n), loss tangent (tan (δ)), irradiation intensity (E_e), and phenolic content (D_{Ph}) as shown in Figure 1d. The Cross Power Law parameters (η_0, m, and n) and loss tangent (tan (δ)) are defined in Figure 1e. The detailed definitions of these rheological parameters are presented in Section 5.2. The construction and preprocessing of the condition vector are depicted in Section 5.4.

2.2. Predictive modelling of rheological parameters and data analysis

SVR models were employed to predict rheological parameters from ALG-Ph and HA-Ph compositions, as

shown in Figure 2a. The Cross Power Law parameters (η_0, m, n) and loss tangent (tan (δ)) were used as target variables. The optimal SVR hyperparameters derived from 10-fold cross-validation (CV) for each rheological parameter are listed in Table 1. The SVR models were used for interpolation within the sampled composition range, but not for extrapolation beyond it. The SVR prediction surfaces for η_0, m, n, and tan (δ) showed smooth, composition-dependent trends and closely matched the fitted empirical data across the explored composition range (ALG-Ph: 0–5.0% (w/v); HA-Ph: 0–3.0% (w/v)), as depicted in Figure 2b–e. The predicted vs. actual plots

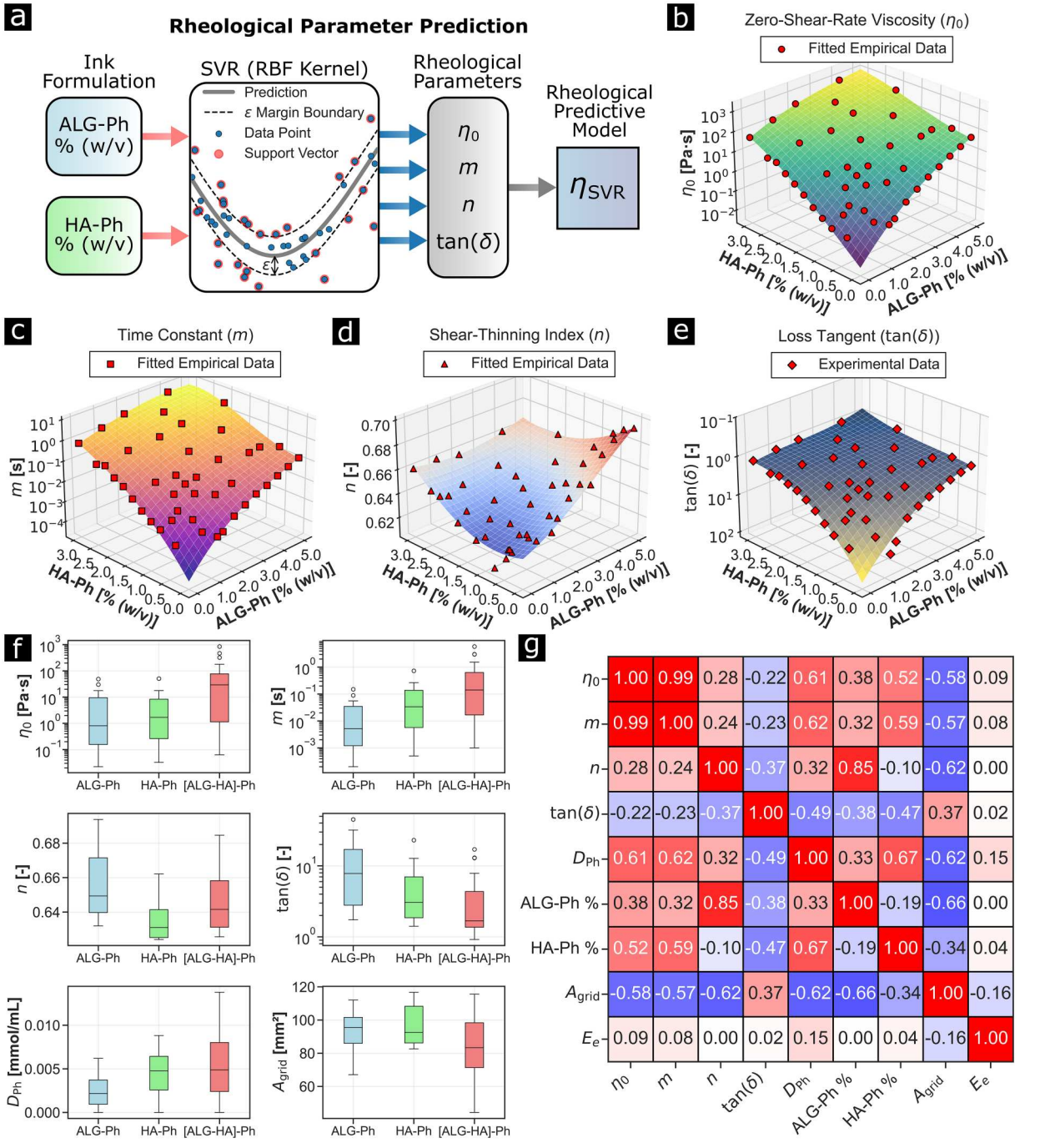

Figure 2. Predictive modelling and data analysis of rheological parameters via support vector regression (SVR). (a) Rheological parameters of [ALG-HA]-Ph composite inks were predicted by SVR models based on ink concentrations. RBF: radial basis function. (b–e) SVR prediction surfaces for (b) zero-shear-rate viscosity (η_0), (c) time constant (m), (d) shear-thinning index (n), and (e) loss tangent (tan (δ)). (f–g) Data analysis based on ink composition (ALG-Ph and HA-Ph concentrations), rheological parameters (η_0, m, n, and tan (δ)), phenolic content (D_{Ph}), irradiation intensity (E_e), and printed grid construct area (A_{grid}) ($n = 766$). (f) Data distribution analysis. (g) Correlation matrix.

Table 1. 10-fold cross-validated optimal SVR hyperparameters for rheological parameters.

Rheological parameter	Regularisation parameter (C)	Kernel coefficient (γ)	Epsilon-tube width (ϵ)
Zero-shear-rate viscosity (η_0)	1673.3	0.025	0.01
Time constant (m)	5000.0	0.04	0.01
Shear-thinning index (n)	10.0	0.04	0.01
Loss tangent ($\tan(\delta)$)	1673.3	0.025	0.085

from 10-fold CV for all rheological parameters are shown in Figure S2. These rheological parameters were evaluated above 0.25% (w/v) ALG-Ph and 0.25% (w/v) HA-Ph for the composite inks, as 0% (w/v) [ALG-HA]-Ph is not well-defined. η_0 and m increased with ink concentration and exhibited similar trends, ranging from 2.6×10^{-2}–1.2×10^{3} Pa·s and 3.1×10^{-4}–6.0×10^{0} s, respectively. n ranged from 0.62–0.69. $\tan(\delta)$ ranged from 32.0–0.68 as the ink concentration increased. At similar ink concentrations, HA-Ph inks exhibited higher η_0, m, but lower n and $\tan(\delta)$ compared to ALG-Ph inks.

The overall experimental data distributions of η_0, m, n, and $\tan(\delta)$, D_{Ph}, and the area of printed grid structures (A_{grid}) under irradiation intensity (E_e) for the ALG-Ph, HA-Ph, and [ALG-HA]-Ph groups were depicted in Figure 2f. E_e is presented as the irradiance strength reading ranging from 0 to 100%; the corresponding spectral irradiation values in W/m^2 are shown in Figure S3. Overall, [ALG-HA]-Ph composite inks exhibited higher η_0, m, and lower $\tan(\delta)$, whereas the ALG-Ph group showed higher n. D_{Ph} ranged from 0 to 1.4×10^{-2} mmol-Ph/mL. For similar concentrations, HA-Ph inks possessed higher D_{Ph} values compared to ALG-Ph inks. A_{grid} ranged from 116.7–44.3 mm^2, with [ALG-HA]-Ph composite inks having noticeably smaller areas. The correlations among all variables were evaluated using Pearson correlation analysis, as shown in Figure 2g. The correlation coefficient (r) ranges from −1.0–1.0, where 1.0 denotes a perfect positive linear relationship, −1.0 denotes a perfect negative linear relationship, and 0 indicates the absence of a linear association. η_0 and m were colinearly correlated ($r=0.99$), and n showed a strong positive correlation ($r=0.85$) with ALG-Ph content and a weak negative correlation ($r=-0.10$) with HA-Ph content, indicating that shear-thinning behaviour was mainly governed by ALG-Ph inks. A_{grid} exhibited moderate negative correlations with η_0, m, n, D_{Ph}, and polymer contents, with a moderate positive correlation with $\tan(\delta)$. A_{grid} and E_e had a weak negative correlation ($r=-0.16$), which suggested that although A_{grid} decreased as E_e increased, the change was not substantial.

2.3. Generative AI modelling of deposition morphology

The detailed architecture of the β-CVAE is depicted in Figure 3a. The CNN-based encoder extracts features from input images and maps them to the parameters $\boldsymbol{\mu}$ and $\log\boldsymbol{\sigma}^2$, which define Gaussian distributions over a 32-dimensional latent space. Latent vectors were sampled from this distribution via the reparameterization trick (Eq. 1) in Section 2.1. The decoder reconstructs images using bilinear upsampling blocks with a sigmoid output. The condition vector c was concatenated both before and after the latent space to enforce condition-dependent generation. Data augmentation via horizontal flipping and rotations was applied to increase the effective size of the training set (Figure 3b). After training, the β-CVAE can generate grid images by sampling the latent prior with prescribed condition vectors (Figure 3c).

To determine a suitable hyperparameter β value that balances realistic generation and high-level disentanglement, a β hyperparameter sweeping was conducted, as shown in Figure 3d. Established disentanglement metrics generally require known ground-truth generative factors, which are not fully defined for the present experimental image dataset [36]. Therefore, formal disentanglement scoring was not directly applicable in this study. Instead, the per-dimension KL divergence was used as a quantitative proxy for latent-space usage. Higher KL divergence indicates an active latent dimension carrying information from the input images, whereas low or near-zero KL divergence indicates an inactive or collapsed dimension close to the prior [37]. $\beta=5$ was chosen since after the 9th most active latent dimension, the KL divergence for the remaining latent space dropped noticeably (KL divergence < 0.5). The latent traversal beyond the 9th most active dimension also showed little or no visual change (Figure S4). An independent test set was prepared to evaluate the model's performance. For each test image, the mean squared error (MSE) between the input and reconstruction was computed. A representative squared-error heatmap is shown in Figure 3e. The filament in the upper right represents the anchoring line for initial ink stabilisation. Furthermore, the distributions of the MSE and the structural similarity index measure (SSIM; a perceptual metric quantifying similarity between two images) across the test set are summarised in Figure 3f, confirming that the trained model generalises to unseen samples while preserving structural content in reconstructed grid geometries. In addition to the MSE and SSIM metrics, predicted vs. actual plots based on printability metrics for evaluating reconstruction

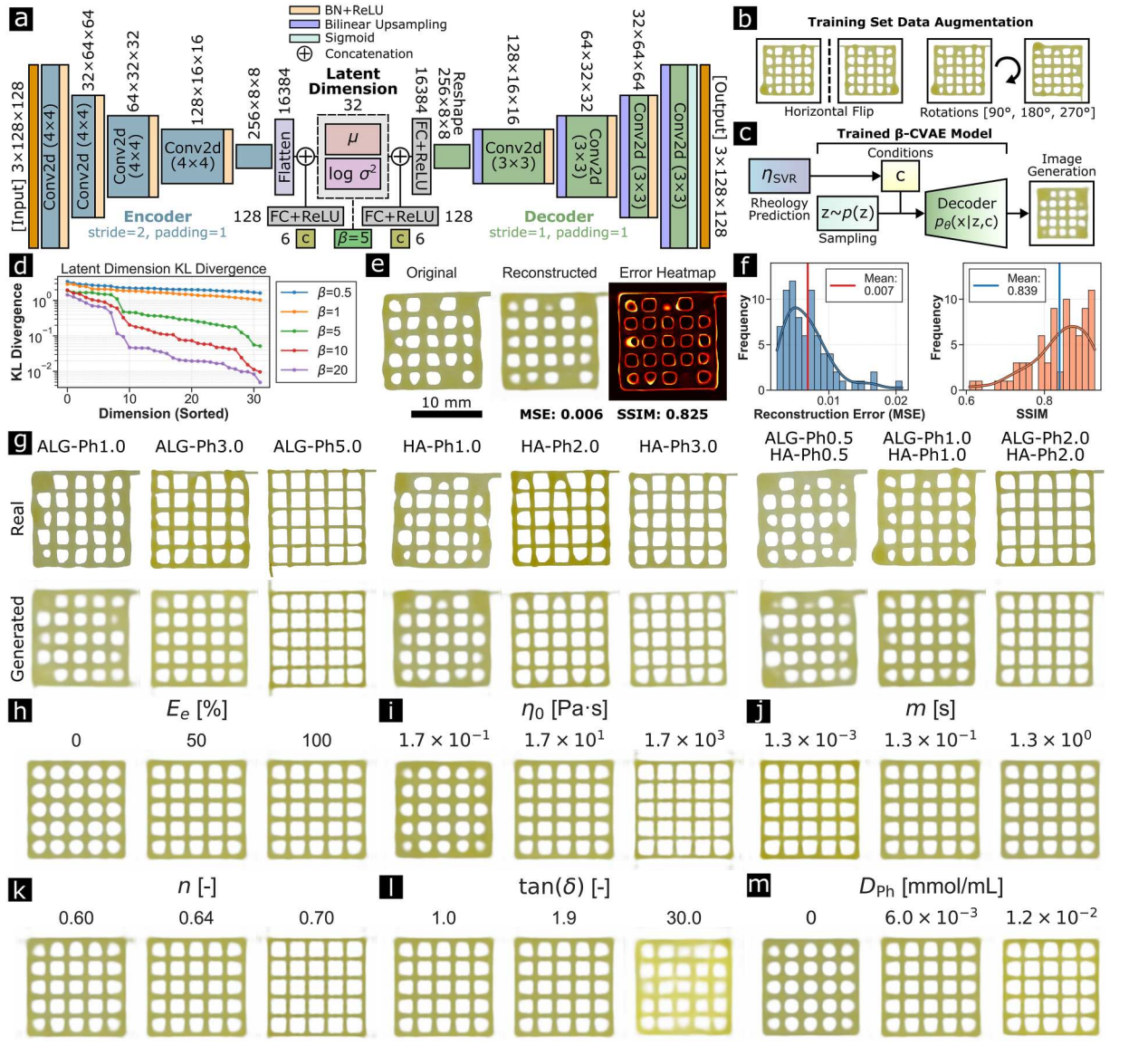

Figure 3. The β-CVAE for generating images of grid structures. (a) Architecture of the β-CVAE model. BN: batch normalisation. ReLU: rectified linear unit. Conv2D: two-dimensional (2D) convolution. FC: fully connected. (b) Data augmentation methods for the training set. (c) Image generation scheme of the β-CVAE. (d) Effect of varying β on the KL divergence of each latent dimension. (e) Heatmap of reconstruction error for a sample in the test set. (f) Distribution of mean squared error (MSE) and structural similarity index measure (SSIM) for the test set ($n = 77$). (g) 3D-printed grid images and β-CVAE-generated images. (h–m) Parameter sweeping of the condition vector: (h) irradiation intensity (E_e), (i) zero-shear-rate viscosity (η_0), (j) time constant (m), (k) shear-thinning index (n), (l) loss tangent ($\tan(\delta)$), and (m) phenolic content (D_{Ph}).

performance are depicted in Figure S5. The training history (reconstruction loss and KL divergence vs. epoch) of the β-CVAE is shown in Figure S6.

For each ink formulation (ALG-Ph, HA-Ph, and [ALG-HA]-Ph), the generated images reproduced the characteristic grid geometry of the corresponding real 3D-printed structures, including filament width, pore openness, and edge roundness (Figure 3g). Morphological differences between the ALG-Ph and HA-Ph inks, as well as the combined behaviour of composite inks, were qualitatively preserved. To examine the effect of individual condition parameters on deposition morphology, a single parameter in the condition vector was swept each time while the remaining were fixed (Figure 3h–m). For each subfigure, the middle image represents the default parameter value. Changes in E_e and D_{Ph} produced a smooth transition from collapsed grids with closed pores at lower values to more rigid structures with thinner filaments and larger pores at higher values. Variations in η_0, m, and n produced gradual changes in filament thickness and pore regularity, indicating a rheological dependency.

Decreasing tan (δ) induced a transition from fluid-like spreading and brighter colour to more elastic filaments that resemble the designed grid geometry.

2.4. Generative diversity and latent space visualisation

To examine generative diversity under fixed rheological conditions, images were generated at selected ink concentrations (ALG-Ph 1–5% (w/v)) at $E_e = 0\%$ and $E_e = 100\%$ using a sampling temperature factor (T) of 0.7 (Figure 4a–c). T is defined in Section 5.5 (Eq. 7); a higher T leads to more chaotic generations, whereas a lower T outputs more deterministic generations. Despite identical condition inputs, the generated images exhibited slight variation in pore morphology, filament thickness, and A_{grid} due to stochastic sampling from the latent space. The distributions of A_{grid} under varying ink concentrations and E_e are shown in Figure 4d. The distributions of A_{grid} for T at 1.0, 0.5, and 0.3 are shown in Figure S7. The overall visual outputs and A_{grid} values nevertheless remained consistent with expected morphological behaviour in experiments.

Real grid images and their corresponding condition vectors were passed through the encoder of the trained β-CVAE to obtain the mean vectors ($\boldsymbol{\mu}$) of the approximate posterior distributions ($q_\phi(\boldsymbol{z}|\boldsymbol{x}, \boldsymbol{c})$), which were then mapped onto a two-dimensional (2D) manifold using uniform manifold approximation and projection (UMAP). UMAP is a nonlinear dimensionality reduction method that preserves local neighbourhood relationships. The UMAP plots showed overall distribution and gradual changes in E_e, $\log(\eta_0)$, $log(1 + D_{Ph})$, and A_{grid} across the manifold (Figure 4e). Localised clusters were observed, including regions dominated by samples printed at low E_e, $\log(\eta_0)$, $\log(1 + D_{Ph})$. For images with low A_{grid}, they were sparsely clustered on the upper right part of the plot, exhibiting higher $\log(\eta_0)$ and $\log(1 + D_{Ph})$. The UMAP plots for $\log(m)$, n, and $\log(\tan(\delta))$ are shown in Figure S8. The correlations of n with other variables were not immediately clear, but images with lower n tended to have higher A_{grid}.

To visualise the feature disentanglement of the latent space, the distribution of a single latent dimension was traversed from −3 to +3 standard deviations (σ). Distributions of all latent dimensions (z0–z31) are depicted in Figure S9. All other latent dimensions were kept fixed, and the corresponding grid images were generated for dimensions z8, z23, and z24 (Figure 4f–h). Changing the latent dimension (z8) produced a systematic change in pore morphology from filled or curled pores (Figure 4f). Variation in another latent dimension (z23) produced gradual changes in the thickness of horizontal and vertical filaments (Figure 4g). Another latent dimension (z24) mainly affected the pixel intensity and area, with lighter grid structures transitioning to darker and more spreading constructs (Figure 4h). The remaining active latent dimension traversals (z1, z30, z29, z27, z10, and z6) are depicted in Figure S10. Representative real grid images that span variations in pore morphology, filament width, and colour intensity are shown in Figure 4i–k. The patterns observed in both the latent traversals and the real printed grids suggest that different latent directions correspond to interpretable physical and geometric features in the real world. Through fixing σ on a particular value, it is possible to manipulate the features in the generated images, such as filament width (z23) (Figure 4l). All generated images ($E_e = 50\%$) exhibited thicker horizontal filament widths at varying ink compositions.

2.5. In silico closed-loop optimisation of deposition morphology

An in silico closed-loop optimisation framework was established by integrating the SVR rheological predictor, β-CVAE image generator, multi-task CNN printability evaluator, and a Bayesian optimiser (Figure 5a). The CNN was trained based on β-CVAE-generated images; the training history and test set evaluation results for the CNN are shown in Figure S11. Candidate ink compositions were mapped to rheological descriptors (η_0, m, n, and tan (δ)) through the SVR model, concatenated with E_e and D_{Ph} to form the condition vector c, and passed to the β-CVAE decoder for image generation. The multi-task CNN evaluated the generated images against the reference blueprint and predicted five printability metrics: filament continuity (completeness), filament width, construct area, Dice similarity coefficient (DSC), and Hausdorff distance (HD) (Figure 5b). These metrics were combined into a weighted objective function described in Section 5.7 (Eq. 10), and the Bayesian optimiser repeatedly updated the condition vector until reaching the iteration threshold.

Representative generated images at $E_e = 50\%$ for ALG-Ph 1.0–5.0% (w/v) and HA-Ph 0.5–3.0% (w/v) exhibited composition-dependent changes in pore openness and filament morphology (Figure 5c). At low polymer concentrations, generated grids showed collapsed pores, while higher concentrations produced finer structures with open pores. The corresponding metric maps revealed distinct patterns across [ALG-HA]-Ph composition (Figure 5d). Completeness probability remained high over a broad region but was low at higher ink concentrations. Construct area decreased as polymer

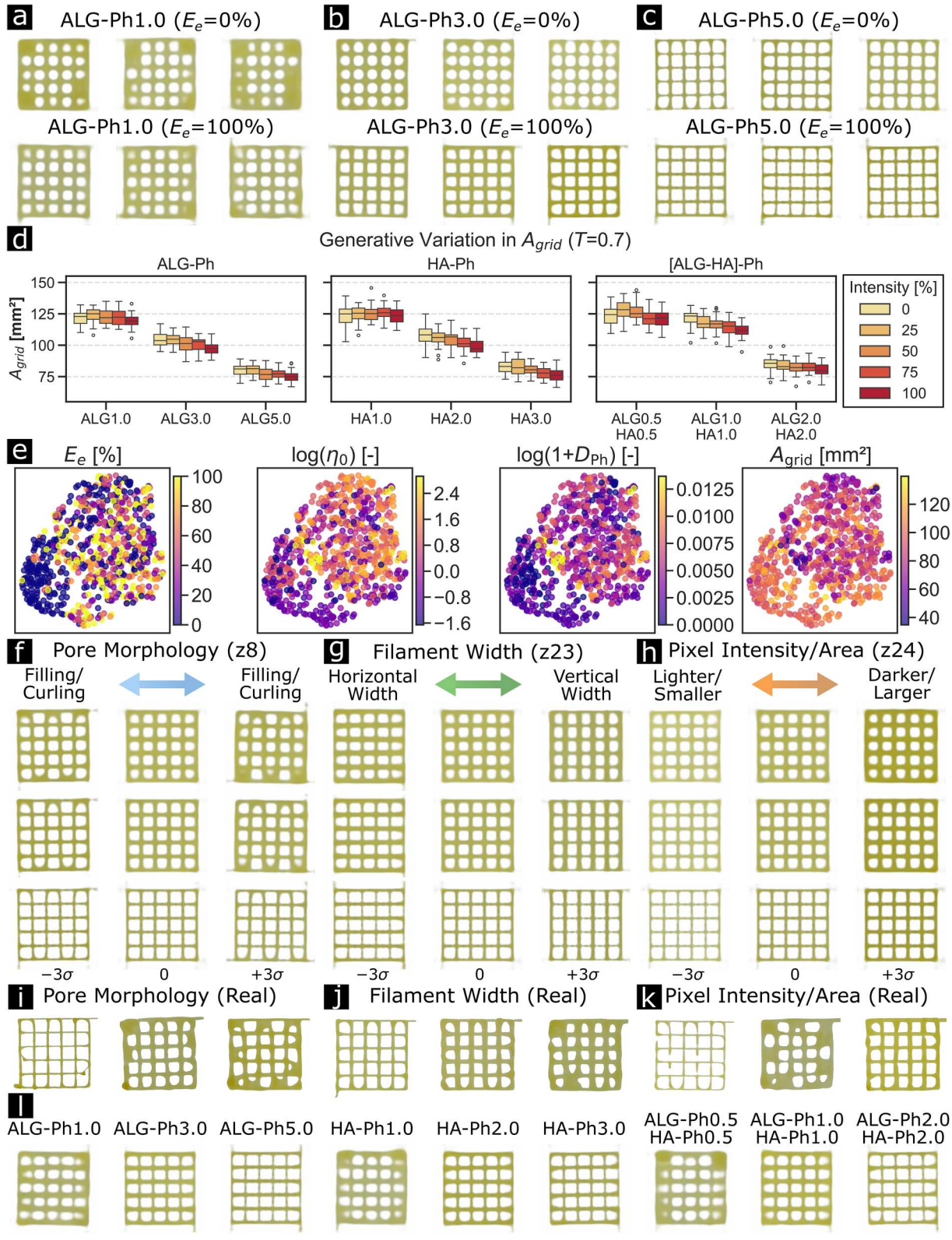

Figure 4. Visualisation of generative diversity and β-CVAE latent space. (a–c) Visual diversity in the generated images with a sampling temperature factor (T) of 0.7. (d) Distributions of A_{grid} when changing ink concentrations and E_e with a T of 0.7 ($n = 30$). (e) Latent vectors of real grid images embedded in 2D space using uniform manifold approximation and projection (UMAP). (f–h) Latent traversals across varying standard deviations (σ) along selected latent dimensions showed systematic changes in pore morphology, filament width, and colour intensity. (i–k) Representative real grids exhibited similar features in the latent space. (l) Latent manipulation by fixing σ on −3 for filament width dimension (z23).

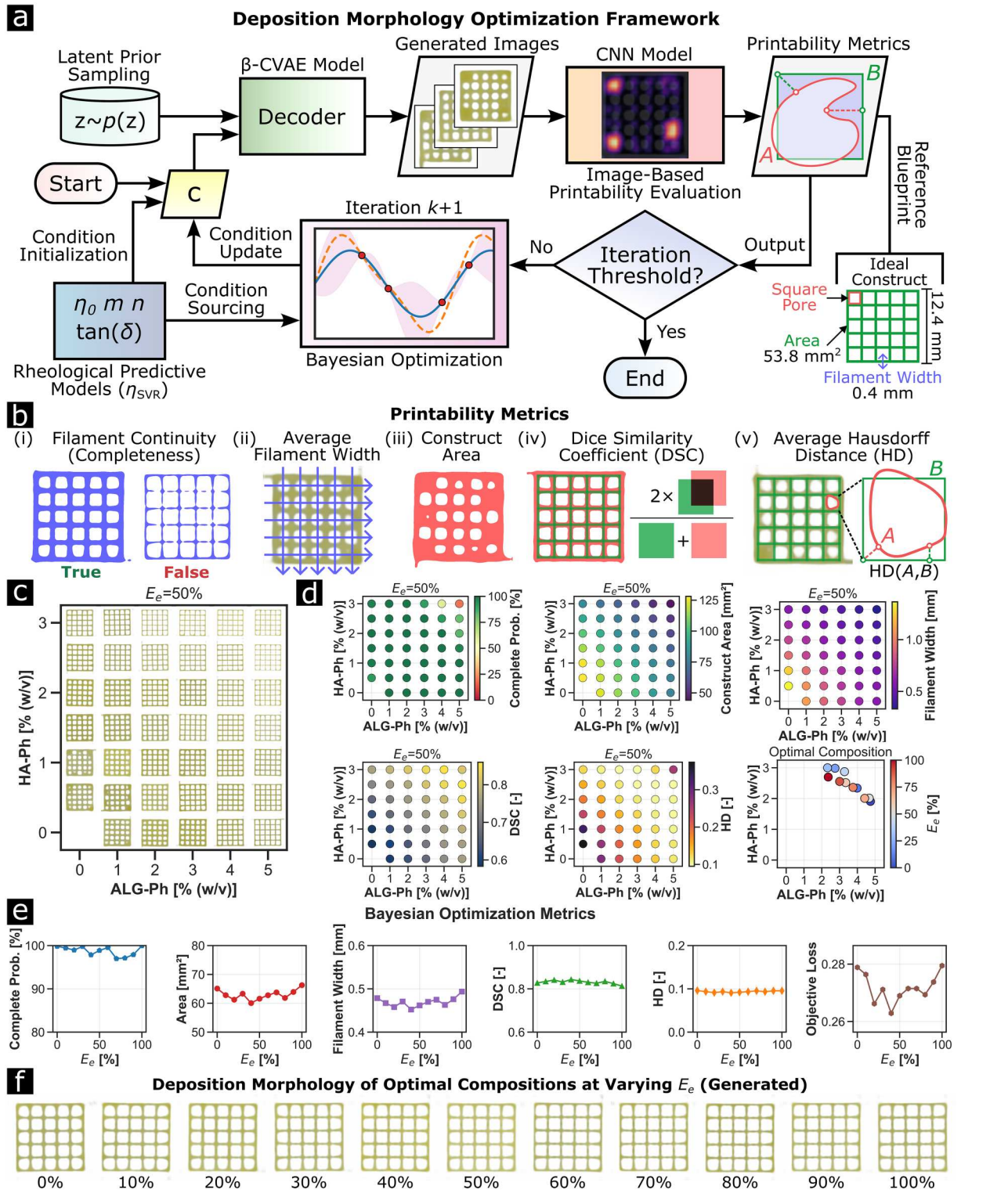

Figure 5. In silico closed-loop optimisation framework for deposition morphology that couples β-CVAE, SVR, CNN, and Bayesian optimisation (BO). (a) Flow chart of the optimisation process. The multi-task CNN scores β-CVAE-generated images using various printability metrics. The score is passed forward to a Bayesian optimiser, which updates the condition vector ***c*** through queries to the SVR rheological model until the iteration threshold is reached. (b) Printability metrics employed in the optimisation framework. (c) Representative images of generated grid structures under varying ALG-Ph and HA-Ph concentrations at $E_e = 50\%$. (d) Metric maps for completeness probability, filament width, A_{grid}, Hausdorff distance (HD), and Dice similarity coefficient (DSC) across the composition space at $E_e = 50\%$ and optimal compositions at varying E_e. (e) BO results showing the evolution of printability metrics and objective loss as a function of E_e. (f) Representative generated images of optimal deposition morphology for each E_e (0–100%).

content increased, whereas filament width showed the opposite trend. DSC and HD showed sharper gradients, with the best geometric accuracy at moderate-to-high polymer concentrations. The optimal compositions identified by the Bayesian optimiser at each irradiation intensity clustered around 3.0–5.0% (w/v) ALG-Ph and 1.0–3.0% (w/v) HA-Ph. The representative generated images and corresponding metric maps at $E_e = 0\%$ and $E_e = 100\%$ are shown in Figure S12.

Bayesian optimisation (BO) across E_e from 0% to 100% maintained completeness probability above 90% throughout the explored range (Figure 5e). The convergence plot of BO for each E_e is shown in Figure S13. Construct area remained relatively stable around 60–70 mm^2, while filament width fluctuated above 0.4 mm and below 0.5 mm. DSC values stayed above 0.8 across all intensities, and HD remained below 0.1, indicating consistent geometric fidelity. The representative images generated under the optimal conditions are shown in Figure 5f. Consistent deposition morphology patterns were observed across E_e.

2.6. New blueprint design adaptation via transfer learning

To extend the applicability of the generative framework, transfer learning was implemented to adapt the pre-trained β-CVAE to new blueprint designs with minimal data (Figure 6a). The encoder and decoder weights trained on grid structures were used as initialisation, and the model was fine-tuned on images of 3D-printed ginkgo leaf, hollow pentagram, and human nose constructs. The fine-tuned β-CVAE can generate realistic images that capture geometry-specific features (Figure 6b–d). For ginkgo leaves, the model reproduced the overall shape, with higher polymer concentrations yielding more defined boundaries. For hollow pentagrams, the generated images preserved the vertices in a manner consistent with the real printed structures. For human noses, the model captured bilateral symmetry despite the increased geometric complexity. Across all blueprints, the generated images closely matched the morphological characteristics of the corresponding real-world constructs.

Parameter sweeping of the condition vector demonstrated that the fine-tuned models retained physically meaningful responses to changes in process and rheological parameters (Figure 6e–f). Increasing E_e produced transitions from collapsed or spread structures to more rigid geometries with high-fidelity edges. Variations in η_0 induced gradual changes in boundary sharpness and structural definition, with higher η_0 yielding improved shape retention. The parameter sweeping results for m, n, $\tan(\delta)$, and D_{Ph} are shown in Figure S14. Decreasing $\tan(\delta)$ resulted in more elastic behaviour and reduced spreading, while increasing D_{Ph} enhanced crosslinking density and structural integrity. Latent traversals along selected active latent dimensions for ginkgo leaf, hollow pentagram, and human nose showed distinct features (Figure S15). Additionally, a graphical user interface (GUI) was developed for the generative AI framework to allow users to input ink compositions and processing variables and to generate on-demand candidates for printing results (Figure 6g).

3. Discussion

This study introduces a conditional generative AI framework for generating novel images of printing outcomes in a visible-light-induced 3D bioprinting system. By conditioning the generative model on rheological parameters (η_0, m, n, and $\tan(\delta)$), irradiation intensity (E_e), and phenolic content (D_{Ph}), images of 3D-printed constructs were generated to match experimental observations. In combination with a multi-task CNN printability evaluator and SVR rheological predictors, this framework can systematically explore and optimise deposition morphologies, thereby reducing the need for trial-and-error experiments.

The visible-light-induced 3D bioprinting system is chosen for its rapid, cytocompatible, and extrusion-synchronized gelation [38]. In this study, crosslinking is achieved via Ru/SPS-mediated phenol coupling which allows temporal crosslinking control by adjusting the irradiation intensity (Figure 1a). Upon visible-light irradiation at 450 nm, photoinitiator $[Ru(bpy)_3]^{2+}$ is excited and transfers an electron to persulfate ($S_2O_8^{2-}$), generating the strong oxidants $[Ru(bpy)_3]^{3+}$ and sulfate radical anions ($SO_4^{\bullet-}$) [34]. These strong oxidants convert phenolic groups on phenol-functionalized polymer (Polymer-Ph) chains into phenoxy radicals, which undergo radical coupling to form covalent crosslinks [39]. This photo-induced crosslinking takes place under mild, liquid conditions and is less vulnerable to oxygen inhibition, allowing for continuous extrusion and quick gelation during printing [40]. The ALG-Ph and HA-Ph composite inks, with 2.0 mM $[Ru(bpy)_3]^{2+}$ and 2.0 mM $Na_2S_2O_8$ under 450 nm visible-light irradiation, fall within previously reported cytocompatible concentration and irradiation ranges for cell-laden constructs [41,42], indicating that the present framework is suitable for 3D bioprinting applications.

As a result, deposition morphology is strongly governed by ink rheology, phenolic content, and irradiation intensity [9,10,43] (Figure 1b). To model this complex bioprinting system, a β-VAE-based generative model is implemented (Figure 1c). Compared to the vanilla

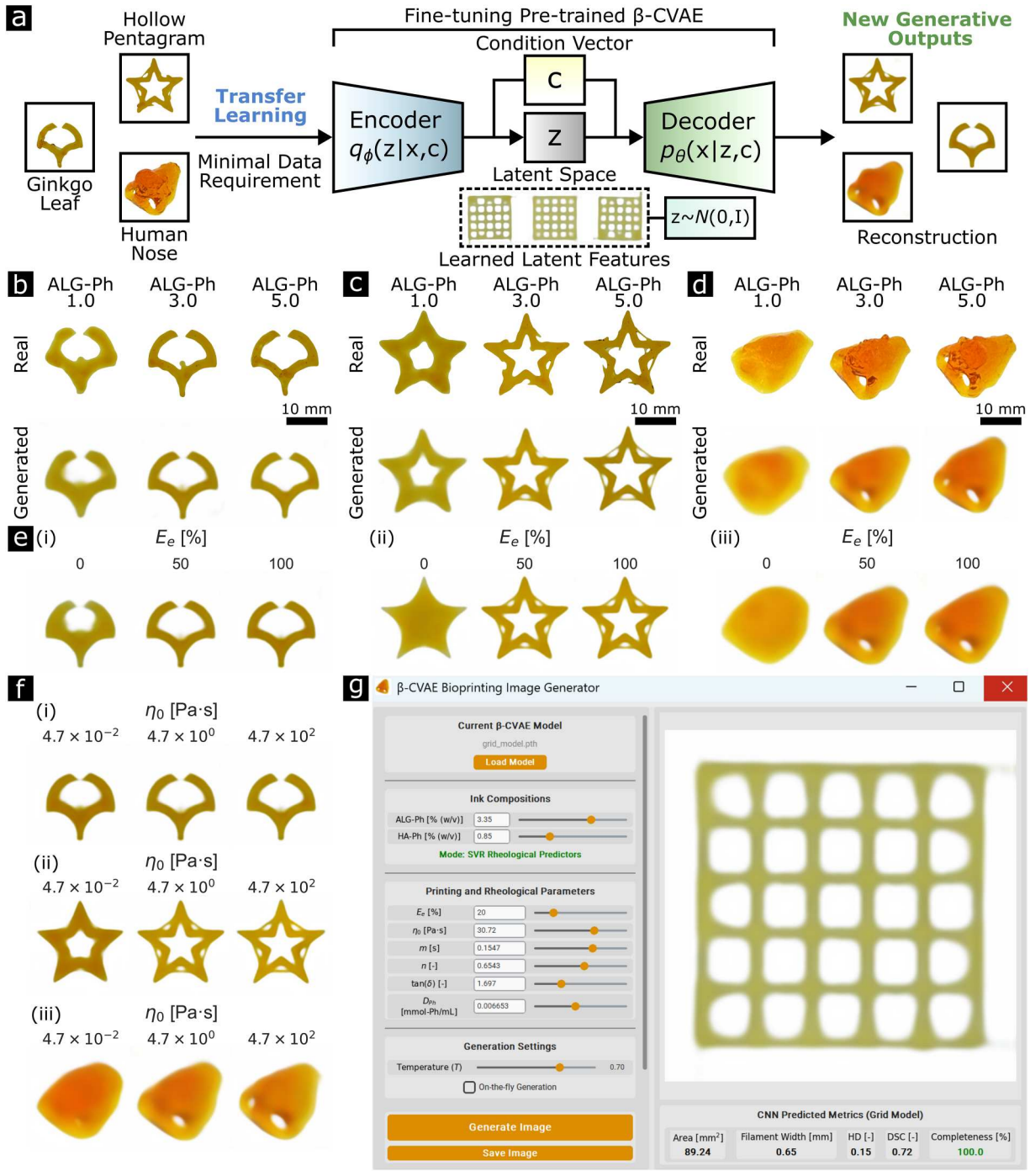

Figure 6. Transfer learning for adapting the pre-trained β-CVAE model to new blueprint designs. (a) Schematic diagram of transfer learning for generating novel blueprint designs, including ginkgo leaf, hollow pentagram, and human nose. (b–d) Real and generated images of (b) ginkgo leaf, (c) hollow pentagram, and (d) human nose constructs at varying ALG-Ph concentrations. (e–f) Parameter sweeping of the condition vector for (e) E_e and (f) η_0: (i) ginkgo leaf, (ii) hollow pentagram, and (iii) human nose. (g) Graphical user interface (GUI) based on β-CVAE models.

variational autoencoder (VAE), β-VAE introduces a regularisation hyperparameter β on the KL divergence term (Eq. 4), which encourages the learning of a disentangled latent space [35]. Such encouragement promotes learning of interpretable latent representations, in which each dimension corresponds to meaningful features in the data [44]. As a result, interpretable control can be achieved through latent traversals, and sensitivity to specific features can be isolated [37]. With the addition of the condition vector, the output of the β-CVAE can be constrained to desired conditions, such as rheological and printing parameters (Figure 1d). The rheological

properties of inks were characterised using the Cross Power Law parameters (Eq. 5) and loss tangent (Eq. 6), which contain physical meanings: η_0 represents apparent viscosity at an extremely low shear rate, m is the critical transitional time for shear-thinning behaviour, n denotes the degree of shear-thinning, and $\tan(\delta)$ describes the elastic and viscous behaviour (Figure 1e).

The SVR predictive models define a quantitative link between ink formulation and rheological parameters (Figure 2a). SVR was selected for its effectiveness in small datasets and its ability to model nonlinear relationships via kernel functions [45]. The prediction surfaces for Cross Power Law parameters (η_0, m, n) and loss tangent ($\tan(\delta)$) captured smooth, composition-dependent trends (Figure 2b–e) which suggests appropriate fittings and generalizability. The distribution of experimental data was diverse and comprehensive, which is critical for the training of generative AI models (Figure 2f). The moderate negative correlations between A_{grid} and both viscosity-related parameters (particularly η_0) and D_{Ph} suggest that multiple mechanisms could contribute to improved shape retention, including resistance to spreading and crosslinking-mediated structural stabilisation (Figure 2g). The effect of E_e on A_{grid} is limited ($r = -0.16$), which can be attributed to the rapid crosslinking kinetics of the Ru/SPS system, where a threshold irradiation level provides sufficient radical generation to initiate gelation [41].

For the β-CVAE, the selection of $\beta = 5$ based on the per-dimension KL divergence analysis is a trade-off between reconstruction loss and latent space disentanglement (Figure 3d). A higher β value encourages stronger regularisation toward the prior distribution, thereby promoting disentanglement but sacrificing reconstruction details [37]. The observation in which only nine latent dimensions remained active ($KL \geq 0.5$) under $\beta = 5$ suggests that the essential morphological variations in the grid dataset can be captured by a relatively compact representation. The MSE (mean = 0.007) and SSIM (mean = 0.839) on the independent test set (Figure 3e–f) confirm that the chosen β achieves good reconstruction and visual appearance while preserving an interpretable latent structure. For each ink formulation, the model accurately reproduced characteristics consistent with the experimentally observed deposition morphology (Figure 3g). When individual elements of the condition vector were swept, the generated grids exhibited smooth, physically plausible transitions (Figure 3h–m). These results indicate that the β-CVAE learned physical meanings of each condition parameter for deposition morphology.

Under the same conditions, the generated images showed minor differences in pore structure and filament appearance. The stochastic nature of generative models (which can be controlled through the sampling temperature factor (T)) enables the AI framework to generate model-sampled variability under fixed conditions (Figure 4a–d). This can support uncertainty-aware screening by generating multiple samples under identical conditions; variations in predicted areas provide an estimate of model-sampled morphological variability, which can guide formulation screening [46]. However, it is important to note that this variability should not be interpreted as direct experimental repeatability without validation using replicate prints under matched conditions; a dedicated dataset containing sufficient replicate prints at identical ink compositions and irradiation intensities would be required to quantitatively compare experimental and generated variability. The UMAP projection of the latent vectors revealed that samples with similar rheological properties and printing parameters were clustered together. At the same time, a distinct region characterised by low E_e conditions emerged (Figure 4e). These structures indicate that the learned manifold organises experimentally relevant deposition patterns into a structured, continuous space. Moreover, latent traversals along selected latent dimensions produced systematic changes in pore filling/curling, filament width, colour intensity, and area (Figure 4f–h), which align with trends observed in the experimental grids (Figure 4i–k). Although it is difficult to immediately associate each latent dimension with a single physical or printing parameter from the visualisation, the presence of disentangled, interpretable directions suggests that the model captures a compact representation of key morphological features. In practice, this allows fixing a particular latent dimension to preserve one aspect of grid morphology while varying the remaining dimensions to explore other aspects (Figure 4l). This can be useful for removing unwanted artifacts or adjusting positions in the generated images.

The in silico closed-loop Bayesian optimisation (BO) system applies the β-CVAE to systematically optimise the ink formulation and deposition morphology (Figure 5a). By combining the generative model with BO, candidate formulations can be efficiently evaluated without physical experiments. The metric maps across the composition space revealed trade-offs between completeness, geometric fidelity, and construct area (Figure 5c–d). A high probability of completeness was achieved across a broad compositional range, but only a narrow region exhibited high printability, as measured by the Dice similarity coefficient (DSC) and the Hausdorff distance (HD). The high stability of printability metrics across irradiation levels (Figure 5e) indicates that optimal conditions for each irradiation intensity yield similar deposition morphologies (Figure 5f); any further

improvement will reduce the probability of completeness. Overall, the framework helps identify ink compositions and operational parameters that increase the likelihood of successful printing.

The transfer learning results demonstrated that latent representations learned from grid structures can be applied to other blueprints in 3D bioprinting (Figure 6a–d). By initialising the encoder and decoder weights from the pretrained model, fine-tuning required substantially fewer samples than training from scratch. The fine-tuned models retained physically meaningful responses to changes in the condition vector (Figure 6e–f), indicating that the underlying structure-property relationships in the condition vector were captured during the previous training. The adaptation to ginkgo leaves, hollow pentagrams, and human noses demonstrates that the framework can meet diverse design needs in tissue engineering applications. Finally, the graphical user interface (GUI) enhances usability by enabling interactive input of conditions and immediate visualisation of generated morphologies (Figure 6g).

Despite these advantages, the present framework is subject to several limitations. The models were trained on 2D images, which limits their ability to capture detailed deformations. To better model volumetric structures, the framework should be expanded to support 3D data formats such as voxel grids and point clouds, and to include new encoder architectures, such as PointNet [47], which can directly process unordered point sets while preserving local geometric features. Additionally, the dataset was limited to the visible-light-induced bioprinting system and a specific set of parameters, which may restrict its applicability to other bioprinting configurations. The current study focused on acellular hydrogel printing and did not account for biological factors such as cell viability and long-term proliferation, which are essential for tissue engineering applications [48]. The closed-loop optimisation was also performed in silico prior to printing and did not provide real-time correction; coupling the trained generative and evaluator models with in situ camera monitoring and layer-by-layer feedback control is an important next step toward true closed-loop optimisation in bioprinting [49]. Future work should incorporate 3D morphology, in situ monitoring with real-time feedback control, and additional variables such as cell viability and proliferation, while diversifying bioinks and system parameters to enhance the robustness and applicability of the generative AI framework for 3D bioprinting.

4. Conclusion

In conclusion, a generative AI-guided framework was created to model and optimise deposition morphology in a visible-light-induced hydrogel printing system intended for 3D bioprinting applications. The β-CVAE model was conditioned on key rheological parameters, irradiation intensity, and phenolic content. The model can rapidly generate realistic, condition-dependent images of printed grid structures while maintaining a disentangled and interpretable latent space. By coupling the generative model with a multi-task CNN-based printability evaluator and SVR rheological predictors, the framework enabled efficient in silico optimisation of ink formulations with fewer experimental iterations. Furthermore, transfer learning was shown to adapt the pretrained β-CVAE model to new blueprint designs with limited training data, highlighting the framework's versatility and generalizability. Although the present study focused on acellular hydrogel printing, the bioink formulations and crosslinking conditions employed are cytocompatible and extensible to 3D bioprinting applications. This novel approach can provide a foundation for data-efficient design and screening tools in 3D bioprinting, facilitating optimisation of bioink and printing conditions.

5. Experimental

5.1. Rheological measurement

Phenol-modified alginate (ALG-Ph; 0.124 mmol-Ph/g) and phenol-modified hyaluronic acid (HA-Ph; 0.294 mmol-Ph/g) were prepared using sodium alginate (ALG-I-1G; mannuronic acid/guluronic acid ratio ≈ 0.7; molecular weight ≈ 70 kDa; Funakoshi Co., Ltd., Tokyo, Japan) and sodium hyaluronate (HA-HQ; molecular weight ≈ 1,200–2,200 kDa; Kewpie Corporation, Tokyo, Japan) based on previous works [50,51]. 0.0–5.0% (w/v) ALG-Ph and 0.0–3.0% (w/v) HA-Ph were dissolved in phosphate-buffered saline (PBS (-); pH = 7.4) to obtain [ALG-HA]-Ph composite inks. Apparent viscosities were measured using a rheometer (HAAKE MARS III; Thermo Fisher Scientific Inc., Waltham, MA, USA) equipped with 40 mm parallel plates over a shear rate range of 0.01–1,000 s^{-1} for 360 s. G' and G'' were measured by applying oscillation-amplitude sweeps within the linear viscoelastic region (LVR) at 1.0 Hz, with a gap size of 0.5 mm, at 22.5 °C.

5.2. Rheological predictor modelling

The shear-rate-dependent viscosity curves of inks were modelled using the Cross Power Law, which is defined as:

$$\eta(\dot{\gamma}) = \eta_{\infty} + \frac{\eta_0 - \eta_{\infty}}{1 + (m\dot{\gamma})^n} \tag{5}$$

where $\dot{\gamma}$ is the shear rate, $\eta(\dot{\gamma})$ is the apparent viscosity as a function of the shear rate, η_{∞} is the infinite-

shear-rate viscosity, η_0 is the zero-shear-rate viscosity, m is the time constant, and n is the shear-thinning index [52]. η_∞ is approximated as a small and constant number at 10^{-3} Pa·s. The loss tangent is calculated based on:

$$\tan(\delta) = \frac{G''}{G'} \tag{6}$$

where G' is the storage modulus, G'' is the loss modulus, and δ is the phase angle.

The Cross Power Law parameters (η_0, m, n) and loss tangent ($\tan(\delta)$) were predicted using SVR based on ink concentrations. SVR models were trained in scikit-learn (version 1.7.0). The SVR dataset contained rheological parameters (η_0, m, n, and $\tan(\delta)$) for 0.0–5.0% (w/v) ALG-Ph and 0.0–3.0% (w/v) HA-Ph composite inks; each rheological parameter contained 45 data points. The data distribution for these rheological parameters is presented in Figure 2f. Logarithmic transformations were applied to η_0, m, and $\tan(\delta)$ to account for wide ranges of values. The input data were standardised to have a mean of zero and a standard deviation of one. SVR models using radial basis function (RBF) kernels were optimised via a 10-fold cross-validation (CV) grid search to find the optimal regularisation parameter (C), kernel coefficient (γ), and epsilon-tube width (ϵ) that minimised MSE. Models were trained using 10-fold CV, and performance was evaluated using R^2, MAE, and RMSE.

5.3. 3D printing

5×5 grid structures (single layer; $12 \times 12 \times 0.4$ mm) were printed using a 3D bioprinter (BIO X; Gen 3; Bico Group, Gothenburg, Sweden) with an extrusion rate of 2.0 µL/s and a horizontal moving speed of 20 mm/s. An anchoring line connected to the grid structure was printed prior to stabilising the initial extrusion. ALG-Ph and HA-Ph containing 2.0 mM tris(2,2′-bipyridyl)ruthenium(II) chloride hexahydrate ($[Ru(bpy)_3]^{2+}$; Tokyo Chemical Industry Co., Ltd., Tokyo, Japan) and 2.0 mM sodium persulfate ($Na_2S_2O_8$; FUJIFILM Wako Pure Chemical Corporation, Osaka, Japan) were extruded through 27-gauge tapered nozzles (tip inner diameter: 0.2 mm; TPND-27G-U; Musashi Engineering, Inc., Tokyo, Japan). During printing, extruded inks were continuously irradiated with a monochromatic blue light source (CL-H1-450-9-1-B; Asahi Spectra Co., Ltd., Tokyo, Japan) at a wavelength of 450 nm with intensities ranging from 0% to 100% (0.001–13.571 W/m^2). After printing, images of the printed constructs were taken immediately. Hollow pentagrams, ginkgo shapes, and human noses were printed under the same conditions as grid structures.

5.4. Data preprocessing

To eliminate background noise and artifacts, the printed structures in the images were segmented using Segment Anything Model 2 (SAM 2; version 2.1) [53] and overlaid on a uniform white background using OpenCV (version 4.10.0). For each sample, irradiation intensity (E_e), zero-shear-rate viscosity (η_0), time constant (m), shear-thinning index (n), phenolic content (D_{Ph}), and loss tangent ($\tan(\delta)$) were assigned to a six-dimensional condition vector; η_0 and m were transformed using a logarithmic transformation due to wide orders of magnitude, D_{Ph} using log1p (the natural logarithm of one plus the input array) to accommodate zero-valued samples, and all condition variables were z-score standardised (zero mean, unit variance) using the mean and standard deviation computed from the training split; the same scaler was applied to the validation, test, and image generation. No manual weights were applied to individual descriptors following standardisation. To examine the relationships among formulation, rheology, and process variables, a Pearson correlation matrix was computed using rheological parameters (η_0, m, n, and $\tan(\delta)$), D_{Ph}, ALG-Ph and HA-Ph concentrations, E_e, and A_{grid}.

5.5. Generative AI modelling

The β-CVAE was implemented in PyTorch (version 2.6.0). The encoder consisted of four 2D convolutional layers (kernel size 4, stride 2) with batch normalisation and rectified linear unit (ReLU) activations, which downsampled 128×128 Red-Green-Blue (RGB) images to 8×8 feature maps. The flattened feature maps were concatenated with a condition embedding obtained by passing the six-dimensional condition vector through a fully connected (FC) layer, and the resulting representation was then mapped to the mean and logarithmic variance of a Gaussian latent distribution ($z \in \mathbb{R}^{32}$). During training, latent variables were sampled using the reparameterization trick (Eq. 1) and concatenated with the condition embedding before being projected to $256 \times 8 \times 8$ feature maps. The decoder consisted of four stages of bilinear upsampling and 3×3 convolutions with batch normalisation and ReLU activations, followed by a final 3×3 convolution with sigmoid activation to reconstruct 128×128 RGB images.

The input images were split into training, validation, and test sets (75/15/10%) before any preprocessing to prevent data leakage (random seed = 42). Models were trained using the Adam optimiser [54] (learning rate: 1×10^{-3}, batch size: 64), with early stopping (patience = 15) based on the validation loss. The objective function combined the mean-squared reconstruction loss with a

β-weighted KL ($\beta = 5$) to promote a disentangled latent representation. Base samples in the training set were augmented by rotations (0°, 90°, 180°, 270°) and horizontal flipping. For inks formulated without sodium persulfate ($Na_2S_2O_8$), an additional condition-space augmentation was applied by pairing the same images with condition vectors at 0% and 100% intensity, with the phenolic content set to 0. The data in the validation and test sets were not augmented. For image generation, latent variables were sampled from a temperature-scaled standard normal prior:

$$\boldsymbol{z} \sim \mathcal{N}(\boldsymbol{0},\ T^2\boldsymbol{I}) \tag{7}$$

with a sampling temperature factor $T = 0.7$ with random seeds of 42. This temperature scaling reduces sampling variance in latent space, yielding more stable and representative grid morphologies while preserving conditional diversity.

5.6. Printability characterisation

The printability of the grid structure is characterised by filament continuity (completeness), average filament width, construct area, average Hausdorff distance (HD) across all pores, and Dice similarity coefficient (DSC).

The grid construct is considered complete when all grid lines are continuous within the reference construct; otherwise, it is incomplete. The average filament width was computed from grid-line widths sampled along horizontal and vertical lines passing through the pore midpoints of the reference construct. The grid construct area is defined as the total foreground area, obtained by thresholding the image to form a binary mask and summing the foreground pixels.

The HD metric was used to quantify the deviation of pores relative to the reference pore within grid structures. The HD between point sets A and B is defined as:

$$\mathrm{HD}(A, B) = \max\{h(A, B), h(B, A)\} \tag{8}$$

where $h(A, B)$ is the largest distance from any point in A to its closest point in B, and $h(B, A)$ is the largest distance from any point in B to its closest point in A. HD between sets A and B is the larger of these two distances.

The DSC metric was used to quantify similarity between the printed grid constructs and the reference. The DSC between sample X and sample Y is defined as:

$$\mathrm{DSC}(X, Y) = \frac{2\,|X \cap Y|}{|X| + |Y|} \tag{9}$$

where X and Y are the sets of foreground pixels in the two samples, $|X|$ and $|Y|$ are the numbers of foreground pixels, and $|X \cap Y|$ is the number of foreground pixels shared by both samples.

A multi-task CNN was trained to predict these metrics from 128×128 grayscale images. The architecture consisted of three convolutional layers (32, 64, and 128 filters, each with 3×3 kernels, ReLU activation, and max pooling), followed by shared dense layers (256 and 128 units) with L2 regularisation (1×10^{-4}). Two output heads were used: a regression head for predicting construct area, filament width, HD, and DSC, and a classification head with sigmoid activation for completeness. The dataset contains β-CVAE-generated images (8,475 samples) and was split into training (70%), validation (20%), and test (10%) sets. Data augmentation was applied to the training set using 4-fold rotations (0°, 90°, 180°, 270°). The model was trained using the Adam optimiser (learning rate = 1×10^{-3}) with early stopping (patience = 20) and learning rate reduction on plateau (factor = 0.5, patience = 10).

5.7. Bayesian optimisation

Bayesian optimisation (BO) was employed to identify the optimal ALG-Ph and HA-Ph concentrations that maximise printability at each irradiation intensity (E_e). BO is a sequential, model-based approach for optimising expensive black-box functions. Given an objective function $f(\boldsymbol{x})$, the goal is to find the optimum $\boldsymbol{x}^* = \arg\min f(\boldsymbol{x})$. In this framework, $\boldsymbol{x}$ = [ALG-Ph % (w/v), HA-Ph % (w/v)] represents the ink composition, and f is the printability loss derived from CNN-predicted metrics on β-CVAE-generated images. A Gaussian process (GP) surrogate model was used to model the objective function and to select new sampling points using the GP-Hedge acquisition strategy. For each E_e interval (0–100%, in 10% increments), the SVR model predicted rheological properties (η_0, m, n, and tan (δ)) from the candidate ink composition, which were then used as conditions for the β-CVAE to generate 30 images (random seed = 42) per evaluation (sampling temperature factor $T = 0.7$). The multi-task CNN evaluated each generated image, and the averaged printability loss was computed as:

$$f(\boldsymbol{x}) = w_{\mathrm{DSC}}(1 - \mathrm{DSC}) + w_{\mathrm{HD}}\,\mathrm{HD} + w_{\mathrm{C}}(1 - p_c) + w_{\mathrm{A}}L_{\mathrm{A}} + w_{\mathrm{W}}L_{\mathrm{W}} \tag{10}$$

where p_c is the predicted completeness probability, L_{A} and L_{W} are normalised quadratic penalties for construct area and filament width (zero when within acceptable ranges of 40–65 mm^2 and 0.3–0.5 mm, respectively), and an additional penalty of 50 was applied when $p_c < 0.5$, and w are the corresponding weights ($w_{\mathrm{DSC}} = 1.0$, $w_{\mathrm{HD}} = 1.0$, $w_{\mathrm{C}} = 5.0$, $w_{\mathrm{A}} = w_{\mathrm{W}} = 1.0$). The BO was conducted using scikit-optimize (version 0.10.2) with 200 iterations to support convergence and 20 initial random samples per intensity level (random seed = 42).

5.8. Transfer learning

Transfer learning was performed by initialising the β-CVAE ($\beta = 5$; condition dimension: 6; latent dimension: 32) with pretrained weights and the condition scaler from the grid model, then fine-tuning on shape-specific datasets for 50 epochs using the Adam optimiser (learning rate $= 1 \times 10^{-3}$, batch size = 16). Data augmentation was applied to expand the limited datasets. For hollow pentagram structures (106 samples), 5-fold rotational symmetry (0°, 72°, 144°, 216°, and 288°) was combined with horizontal flipping. For ginkgo structures (69 samples), horizontal flipping was applied. For human noses (90 samples), 4 rotations within ±15° were applied.

Acknowledgements

Colin Zhang acknowledges support from the Japanese Ministry of Education, Culture, Sports, Science and Technology.

Author contributions

CRediT: **Colin Zhang:** Conceptualization, Data curation, Formal analysis, Investigation, Methodology, Software, Validation, Visualization, Writing – original draft, Writing – review & editing; **Kelum Chamara Manoj Lakmal Elvitigala:** Conceptualization, Data curation, Investigation, Methodology, Writing – review & editing; **Shinji Sakai:** Conceptualization, Funding acquisition, Methodology, Project administration, Resources, Supervision, Writing – review & editing.

Disclosure statement

No potential conflict of interest was reported by the author(s).

Funding

This work was funded by the Adaptable and Seamless Technology Transfer Program through Target-driven R&D (A-STEP) from the Japan Science and Technology Agency (JST) [grant number JPMJTR234C].

Data availability statement

The data that support the findings of this study are openly available in Zenodo at https://doi.org/10.5281/zenodo.19602891, reference number [19602891].

Code availability statement

The scripts used for data analysis and machine learning models in this study are available on GitHub at: https://github.com/KORINZ/generative-ai-bioprinting-framework.

ORCID

Colin Zhang http://orcid.org/0009-0009-2411-9640
Kelum Chamara Manoj Lakmal Elvitigala http://orcid.org/0000-0002-9649-0635
Shinji Sakai http://orcid.org/0000-0002-1041-4798

References

[1] Groll J, Boland T, Blunk T, et al. Biofabrication: reappraising the definition of an evolving field. Biofabrication. 2016;8:013001, doi:10.1088/1758-5090/8/1/013001
[2] Calafel MI, Criado-Gonzalez M, Aguirresarobe R, et al. From rheological concepts to additive manufacturing assessment of hydrogel-based materials for advanced bioprinting applications. Mater Adv. 2025;6:4566–4597. doi:10.1039/D5MA00019J
[3] Ng WL, Vyas C, Huang B, et al. Advanced bioprinting strategies for fabrication of biomimetic tissues and organs. Int J Extreme Manuf. 2025;7:062006, doi:10.1088/2631-7990/adeee0
[4] Zhang YS, Haghiashtiani G, Hübscher T, et al. 3D extrusion bioprinting. Nat Rev Methods Primer. 2021;1:1–20. doi:10.1038/s43586-021-00073-8
[5] Koons GL, Diba M, Mikos AG. Materials design for bone-tissue engineering. Nat Rev Mater. 2020;5:584–603. doi:10.1038/s41578-020-0204-2
[6] Gao X, Chen J, Zhang X, et al. 3D bioprinting for personalized medicine: advances, challenges, and future directions. ACS Biomater Sci Eng. 2025; doi:10.1021/acsbiomaterials.5c00740
[7] Stankey PP, Kroll KT, Ainscough AJ, et al. Embedding biomimetic vascular networks via coaxial sacrificial writing into functional tissue. Adv Mater. 2024;36:2401528, doi:10.1002/adma.202401528
[8] Xu Y, Sarah R, Habib A, et al. Constraint based Bayesian optimization of bioink precursor: a machine learning framework. Biofabrication. 2024;16:045031, doi:10.1088/1758-5090/ad716e
[9] Gillispie G, Prim P, Copus J, et al. Assessment methodologies for extrusion-based bioink printability. Biofabrication. 2020;12:022003, doi:10.1088/1758-5090/ab6f0d
[10] Schwab A, Levato R, D'Este M, et al. Printability and shape fidelity of bioinks in 3D bioprinting. Chem Rev. 2020;120:11028–11055. doi:10.1021/acs.chemrev.0c00084
[11] Paxton N, Smolan W, Böck T, et al. Proposal to assess printability of bioinks for extrusion-based bioprinting and evaluation of rheological properties governing bioprintability. Biofabrication. 2017;9:044107, doi:10.1088/1758-5090/aa8dd8
[12] Barreiro Carpio M, Gonzalez Martinez E, Dabaghi M, et al. High-Fidelity extrusion bioprinting of Low-printability polymers using carbopol as a rheology modifier. ACS Appl Mater Interfaces. 2023;15:54234–54248. doi:10.1021/acsami.3c10092
[13] Ng WL, Chan A, Ong YS, et al. Deep learning for fabrication and maturation of 3D bioprinted tissues and organs. Virtual Phys Prototyp. 2020;15:340–358. doi:10.1080/17452759.2020.1771741
[14] Fareez UNM, Naqvi SAA, Mahmud M, et al. Computational fluid dynamics (CFD) analysis of bioprinting. Adv Healthc Mater. 2024;13:2400643, doi:10.1002/adhm.202400643

[15] Zhang Z, Zhou X, Fang Y, et al. AI-driven 3D bioprinting for regenerative medicine: from bench to bedside. Bioact Mater. 2025;45:201–230. doi:10.1016/j.bioactmat.2024.11.021

[16] Göhl J, Markstedt K, Mark A, et al. Simulations of 3D bioprinting: predicting bioprintability of nanofibrillar inks. Biofabrication. 2018;10:034105, doi:10.1088/1758-5090/aac872

[17] Song K, Zhang D, Yin J, et al. Computational study of extrusion bioprinting with jammed gelatin microgel-based composite ink. Addit Manuf. 2021;41:101963, doi:10.1016/j.addma.2021.101963

[18] Hidaka M, Kojima M, Zhang C, et al. Experimental and numerical approaches for optimizing conjunction area design to enhance switching efficiency in single-nozzle multi-ink bioprinting systems. Int J Bioprinting. 2024;10:4091, doi:10.36922/ijb.4091

[19] Robazzi JVS, Derman ID, Gupta D, et al. The synergy of artificial intelligence and 3D bioprinting: unlocking New frontiers in precision and tissue fabrication. Adv Funct Mater. 2026;36:e09530, doi:10.1002/adfm.202509530

[20] Jin Z, Zhang Z, Shao X, et al. Monitoring anomalies in 3D bioprinting with deep neural networks. ACS Biomater Sci Eng. 2023;9:3945–3952. doi:10.1021/acsbiomaterials.0c01761

[21] Kelly D, Sergis V, Ventura i Blanco L, et al. Autonomous control of extrusion bioprinting using convolutional neural networks. Adv Funct Mater. 2025;35:2424553, doi:10.1002/adfm.202424553

[22] Zhang C, Elvitigala KCML, Sakai S. AI-powered printability evaluation framework for 3D bioprinting using Hausdorff distance metrics. Biofabrication. 2026;18:015015, doi:10.1088/1758-5090/ae288c

[23] Tseng W-C, Liao C-Y, Chassagne L, et al. An ink-insensitive deep learning model for improving the printing quality in extrusion-based bioprinting. Int J Bioprinting. 2024;11:599–614. doi:10.36922/ijb.6701

[24] Quan R, Liu F, Chinchilla SC. Integrating machine learning and finite element simulation for interpretable prediction of 3D-printed bone scaffold mechanics. Int J Bioprinting. 2025;11:327–348. doi:10.36922/IJB025270257

[25] Jumper J, Evans R, Pritzel A, et al. Highly accurate protein structure prediction with AlphaFold. Nature. 2021;596:583–589. doi:10.1038/s41586-021-03819-2

[26] Teo ZL, Thirunavukarasu AJ, Elangovan K, et al. Generative artificial intelligence in medicine. Nat Med. 2025;31:3270–3282. doi:10.1038/s41591-025-03983-2

[27] Tiwary P, Herron L, John R, et al. Generative AI for computational chemistry: A roadmap to predicting emergent phenomena. Proc Natl Acad Sci. 2025;122:e2415655121, doi:10.1073/pnas.2415655121

[28] Park J, Noh J, Shin J, et al. Investigating static and dynamic behaviors in 3D chiral mechanical metamaterials by disentangled generative models. Adv Funct Mater. 2025;35:2412901, doi:10.1002/adfm.202412901

[29] Kossale Y, Airaj M, Darouichi A. Mode collapse in generative adversarial networks: An overview, in: 2022 8th Int. Conf. Optim. Appl. ICOA. 2022: 1–6. doi:10.1109/ICOA55659.2022.9934291.

[30] Kingma DP, Welling M. Auto-encoding variational bayes, 2013. doi:10.48550/arXiv.1312.6114.

[31] Wang D, Wang Y, Evans L, et al. From latent dynamics to meaningful representations. J Chem Theory Comput. 2024;20:3503–3513. doi:10.1021/acs.jctc.4c00249

[32] Lim J, Ryu S, Kim JW, et al. Molecular generative model based on conditional variational autoencoder for de novo molecular design. J Cheminformatics. 2018;10:31, doi:10.1186/s13321-018-0286-7

[33] Lee M, Min K. Mgcvae: multi-objective inverse design via molecular graph conditional variational autoencoder. J Chem Inf Model. 2022;62:2943–2950. doi:10.1021/acs.jcim.2c00487

[34] Wu Z, Wang J, Huang D, et al. Ultrahigh cell density 3D bioprinting by acoustic fluids-mediated stereolithography. Adv Mater. 2026;38:e11418, doi:10.1002/adma.202511418

[35] Higgins I, Matthey L, Pal A, et al. Beta-VAE: Learning basic visual concepts with a constrained variational framework, in: 2017. https://openreview.net/forum?id=Sy2fzU9gl (accessed July 23, 2025).

[36] Locatello F, Tschannen M, Bauer S, et al. Disentangling factors of variation using few labels, 2020. doi:10.48550/arXiv.1905.01258.

[37] Burgess CP, Higgins I, Pal A, et al. Understanding disentangling in β-VAE, 2018. doi:10.48550/arXiv.1804.03599.

[38] Zheng Z, Eglin D, Alini M, et al. Visible light-induced 3D bioprinting technologies and corresponding bioink materials for tissue engineering. A Review, Engineering. 2021;7:966–978. doi:10.1016/j.eng.2020.05.021

[39] Kim H, Kang B, Cui X, et al. Light-Activated decellularized extracellular matrix-based bioinks for volumetric tissue analogs at the centimeter scale. Adv Funct Mater. 2021;31:2011252, doi:10.1002/adfm.202011252

[40] Lim KS, Schon BS, Mekhileri NV, et al. New visible-light photoinitiating system for improved print fidelity in gelatin-based bioinks. ACS Biomater Sci Eng. 2016;2:1752–1762. doi:10.1021/acsbiomaterials.6b00149

[41] Sakai S, Kamei H, Mori T, et al. Visible light-induced hydrogelation of an alginate derivative and application to stereolithographic bioprinting using a visible light projector and acid Red. Biomacromolecules. 2018;19:672–679. doi:10.1021/acs.biomac.7b01827

[42] Kotani T, Hananouchi T, Sakai S. Enhancing visible light-induced 3D bioprinting: alternating extruded support materials for bioink gelation. Biomed Mater. 2025;20:035005, doi:10.1088/1748-605X/adc0d6

[43] Khanmohammadi M, Nemati S, Ai J, et al. Multipotency expression of human adipose stem cells in filament-like alginate and gelatin derivative hydrogel fabricated through visible light-initiated crosslinking. Mater Sci Eng C. 2019;103:109808, doi:10.1016/j.msec.2019.109808

[44] Kim H, Mnih A. Disentangling by factorising, 2019. doi:10.48550/arXiv.1802.05983.

[45] Chowdhury C. Exploring quantum support vector regression for predicting hydrogen storage capacity of nanoporous materials. Adv Intell Discov. 2025: e202500015, doi:10.1002/aidi.202500015

[46] Edupuganti V, Mardani M, Vasanawala S, et al. Uncertainty quantification in deep MRI reconstruction. IEEE Trans Med Imaging. 2021;40:239–250. doi:10.1109/TMI.2020.3025065

[47] Qi CR, Su H, Mo K, et al. PointNet: Deep learning on point sets for 3D classification and segmentation, 2017. doi:10.48550/arXiv.1612.00593.

[48] Ng WL, Bartolo P. 3D bioprinting of tissues and organs for systemic diseases and localized injuries. Mil Med Res. 2026;13:100006, doi:10.1016/j.mmr.2026.100006
[49] Chen H, Huang J. Advancing sustainability in bioprinting through artificial intelligence. Int J Bioprinting. 2025;11:133–153. doi:10.36922/IJB025170164
[50] Sakai S, Kawakami K. Synthesis and characterization of both ionically and enzymatically cross-linkable alginate. Acta Biomater. 2007;3:495–501. doi:10.1016/j.actbio.2006.12.002
[51] Elvitigala KCML, Mohan L, Mubarok W, et al. Phototuning of hyaluronic-acid-based hydrogel properties to control network formation in human vascular endothelial cells. Adv Healthc Mater. 2024;13:2303787, doi:10.1002/adhm.202303787
[52] Zhang C, Elvitigala KCML, Mubarok W, et al. Machine learning-based prediction and optimisation framework for as-extruded cell viability in extrusion-based 3D bioprinting. Virtual Phys Prototyp. 2024;19:e2400330, doi:10.1080/17452759.2024.2400330
[53] Ravi N, Gabeur V, Hu Y-T, et al. SAM 2: Segment anything in images and videos, 2024. doi:10.48550/arXiv.2408.00714.
[54] Kingma DP, Ba J. Adam: A method for stochastic optimization, 2017. doi:10.48550/arXiv.1412.6980.